Design and Simulation of a Ring-Shaped Linear Array for Microultrasound Capsule Endoscopy

Holly S. Lay, *Member, IEEE*, Benjamin F. Cox, Vipin Seetohul, *Member, IEEE*, Christine E. M. Démoré, *Member, IEEE*, and Sandy Cochran, *Member, IEEE*

***Abstract*— Video capsule endoscopy (VCE) has significantly advanced visualization of the gastrointestinal tract since its introduction in the last 20 years. Work is now under way to combine VCE with microultrasound imaging. However, small maximum capsule dimensions, coupled with the electronics required to integrate ultrasound imaging capabilities, pose significant design challenges. This paper describes a simulation process for testing transducer geometries and imaging methodologies to achieve satisfactory imaging performance within the physical limitations of the capsule size and outlines many of the tradeoffs needed in the design of this new class of ultrasound capsule endoscopy (USCE) device. A hybrid MATLAB model is described, incorporating Krimholtz-Leedom-Matthaei circuit elements and digitizing and beamforming elements to render a gray-scale B-mode. This model is combined with a model of acoustic propagation to generate images of point scatterers. The models are used to demonstrate the performance of a USCE transducer configuration comprising a single, unfocused transmit ring of radius 5 mm separated into eight segments for electrical impedance control and a 512-element receive linear array, also formed into a ring. The MATLAB model includes an ultrasonic pulser circuit connected to a piezocrystal composite transmit transducer with a center frequency of 25 MHz. B-scan images are simulated for wire target phantoms, multilayered phantoms, and a gut wall model. To demonstrate the USCE system's ability to image tissue, a digital phantom was created from single-element ultrasonic transducer scans of porcine small bowel *ex vivo* obtained at a frequency of 45 MHz.**

***Index Terms*— Capsule endoscopy, endoscopic ultrasound (EUS), gastrointestinal (GI) tract, high-resolution ultrasound, Krimholtz-Leedom-Matthaei (KLM), system modeling, ultrasound circuits.**

I. Introduction

ENDOSCOPIC visualization of the gastrointestinal (GI) tract has been practiced for over 200 years, with recent developments including fiber-optic light sources and high-definition cameras [1]. Video capsule endoscopy (VCE) was introduced into clinical practice in the past 20 years and has established itself particularly in diagnosis of small bowel disorders [2]. The small dimensions and minimally invasive nature of VCE make it safe, convenient for the patient, and able to image the remote, elongated and convoluted small bowel without the need for an insertion tube or tether.

Despite VCE's proven utility, it has a number of deficiencies that prevent it finding more use by gastroenterologists. A particularly important issue is that conventional optical imaging allows viewing only of the surface of the GI tract. Optical coherence tomography allows penetration beneath the tissue surface, but it is depth limited and still at an early stage of development [3]. Fluorescence imaging is another optical technique that may expand the range of medical indications that can be addressed and it has also been proposed that imaging with microultrasound (μUS) could provide enhanced information on optically obscure diseases [4].

The topic considered in this paper is μUS imaging of the GI tract itself. Whilst endoscopic ultrasound (EUS) imaging is now common, clinical ultrasound capsule endoscopy (USCE) has not yet been implemented successfully [2]. There are two possibilities for USCE, one to replicate the use of EUS imaging beyond the GI tract and the other to image the wall of the GI tract. The second possibility complements VCE in diagnosis of GI tract disorders and is likely to be used in devices combining VCE and USCE to meet clinicians demands. For this application, it is important to be able to distinguish the multiple layers of tissue within the wall of the GI tract and to determine their characteristics [5]. Since the layers are relatively thin (1–2 mm maximum), subsurface but still only superficial imaging is required. Although μUS signal attenuation with depth is often assumed to be prohibitive, the limited tissue penetration required makes capsule-based μUS imaging of the wall of the GI tract a viable technique [6].

Despite its potential, work to date on implementation of USCE has been limited, see [7]–[10]. However, the choice between mechanically scanned (rotating) and array-based solutions has already arisen. Array-based systems now dominate use in diagnostic ultrasound, with mechanically scanned systems used only in niche applications. Mechanical scanning simplifies electronics and is therefore particularly attractive for USCE in its initial development [8], [9], [11]. USCE also has parallels with intravascular ultrasound (IVUS) in which side-looking circular transducer arrays generating radial images are now relatively common [12]–[15] and it is this configuration that is considered here and in [16].

Because of the complexity of manufacturing the highly miniaturized arrays needed for μUS, detailed modeling is needed to study designs that offer the best possibility of

Manuscript received September 29, 2017; accepted January 9, 2018. Date of publication January 15, 2018; date of current version March 30, 2018. This work was supported by the U.K. Engineering and Physical Sciences Research Council under its Sonopill Programme (EP/K034537). *(Corresponding author: Holly S. Lay.)*

H. S. Lay and S. Cochran are with the University of Glasgow, Glasgow G12 8QQ, U.K. (e-mail: holly.lay@glasgow.ac.uk; sandy.cochran@glasgow.ac.uk).

B. F. Cox is with the ISN Laboratory—MSI 4, Cell and Developmental Biology, School of Life Sciences, University of Dundee, Dundee DD1 5EH, U.K. (e-mail: b.cox@dundee.ac.uk).

V. Seetohul is with Micrima Ltd, Bristol BS2 0EL, U.K. (e-mail: seetohul@gmail.com)

C. E. M. Démoré is with the Sunnybrook Research Institute, University of Toronto, Toronto, ON M4N 3M5, Canada (e-mail: cdemore@sri.utoronto.ca).

Digital Object Identifier 10.1109/TUFFC.2018.2794220

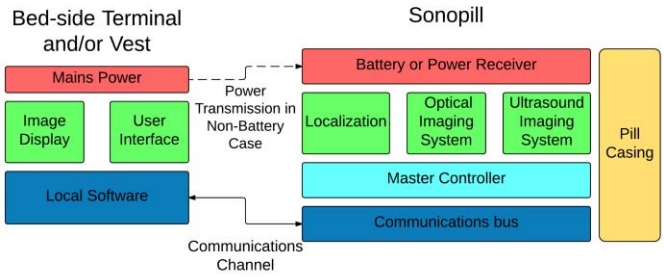

Fig. 1. System components and data flow for the proposed Sonopill capsule. Subsystems are color coded by function: red represents power; light blue represents integrated electronics; dark blue represents the system interface and communications; green represents key functional subsystems; and beige represents physical integration components.

viable images upon physical prototyping and it is this that is considered here. While finite-element analysis (FEA) can well replicate the full physical characteristics of a transducer design, it suffers from long simulation times and high computational expense when applied to USCE because of the need for high array element counts and geometric features with microscopic length scales in mesoscale devices. Previous work has shown good agreement between simpler, 1-D models [17] such as Krimholtz-Leedom-Matthaei (KLM) and prototype devices [18]–[20], allowing a much larger design space to be explored in a reasonable time and it is this approach we describe here.

In Section II, the development of a specification for an array-based USCE system is described. The ultrasound system model is detailed in Section III then two sections describe system design, Section IV relating to the array design and Section V to the digital beamformer. Section VI presents the results of the full system simulation and Section VII includes discussion and conclusions.

II. USCE Imaging System Context

As well as ultrasound, the proposed USCE device is designed to incorporate a suite of complementary sensors with diagnostic capabilities to enhance its potential use in clinical practice. The resulting complexity requires careful system-level design to allow all subsystems to operate without mutual interference. Fig. 1 shows key components of the capsule concept. For tissue assessment and disease diagnosis, both optical and μUS imaging systems are included, as optical systems represent the current clinical standard to be enhanced by the addition of ultrasound. A localization system is needed to record the position in the GI tract of diseased tissue identified by the imaging systems so that it can be located later for monitoring or treatment. Communications systems are required on both the capsule and the base unit to coordinate the image and localization data as well as power systems to monitor and control power usage. Finally, a user interface and image display software will need to be tailored to present the data in a clinically appropriate manner.

The clinical requirements for the capsule impose restrictions on its total size. For both wireless and tethered capsules, the limiting parameter is the need for the patient to swallow the capsule. While there is an absence of the literature on patient preferences during swallowing, the system proposed here is designed with an outer diameter (o.d.) of 10 mm and a length of 30 mm, matching the largest available conventional pharmaceutical pills and within the envelope established by VCE [21]. Because of the limited space for electronics in such a small volume, an application-specific integrated circuit (ASIC) is needed to handle the analog data preprocessing along with master data flow control and data transmission and reception capabilities. This must be matched with complementary hardware on the main display platform. Here, only the ultrasound components are considered in detail but it is important to recognize that they cannot be used in isolation.

The physical dimensions of the capsule also affect the choice of ultrasonic array configuration. Previous work on USCE investigated the use of a rotating single-element transducer [7], [8], and this approach remains under investigation. However, as noted earlier, an array-based approach is reported here as it is expected to provide increased reliability and higher image quality through capabilities such as variable focal depth. For USCE, it is assumed that the array will be constructed to match the outside surface of the capsule geometrically. For the current system design, a side-looking circumferential array is proposed since this can provide complete coverage into the thickness of the wall of the gut without requiring rotation during natural passage of the capsule.

As the proposed capsule is significantly more complex than those currently in use, a corresponding increase in power consumption is expected. Current clinical capsules are designed with a 20-mW power budget based on battery supply limits [2]. To expand this power limit, work is under way on wireless power delivery. However, this leads to concerns about thermal behavior. To address these, trial capsules were designed and manufactured to determine a viable power budget [22]. These capsules used a set of external thermistors and internal temperature sensors to determine the heating caused by various currents flowing through a power resistor. Based on the results of *in vivo* porcine trials, a maximum power budget of 100 mW was established for the proposed design. Numerous techniques to reduce the power consumed below this level are possible, including reduced image frame rate during periods when the capsule is moving only slowly.

III. Ultrasonic System Modeling

Since USCE involves highly complex prototype fabrication, it is necessary to explore possible designs with full ultrasound system simulation. Crucially, this allows assessment of imaging resolution, particularly at small f-numbers. A simulation program was desired which would allow assessment of the system's ability to distinguish thin tissue layers, a key capability for diagnostic use. Simulation is also needed to provide sufficiently accurate electrical characteristics to inform the electronic design, not just of the test circuitry but also of the ASIC at the heart of the entire capsule system. For calculation of electrical characteristics and full tissue phantom simulation, a decision was made to use a 1-D model rather than FEA, saving computation and reducing the feedback time between engineer and clinician. Care was also taken

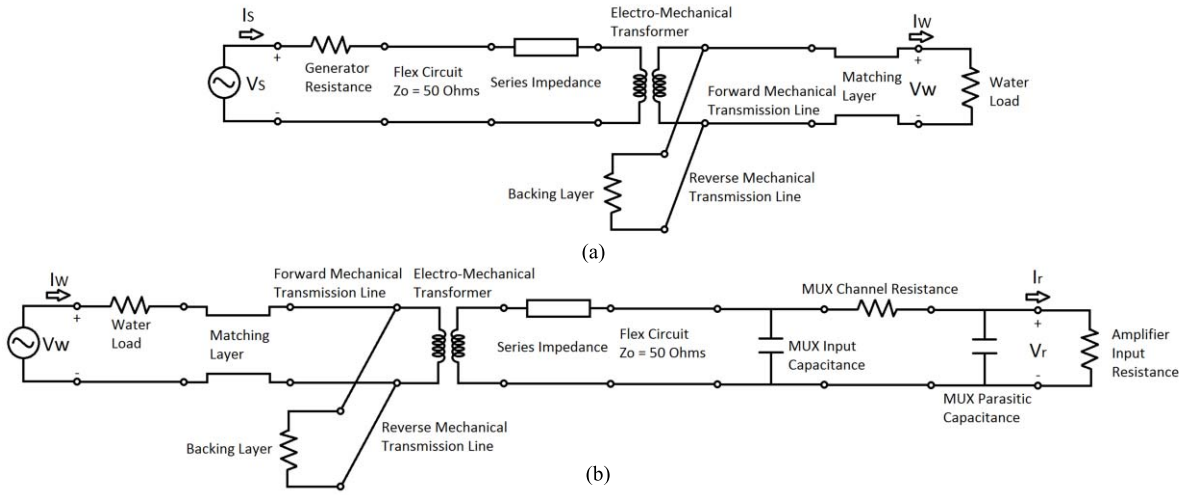

Fig. 2. Full KLM models for the (a) tx and (b) rx circuits. Voltage and current conventions for the KLM system definition have been labeled accordingly.

TABLE I
KLM SIMULATION PARAMETERS

System Component	KLM Implementation	Dimensions	Impedance
Generator Resistance	Series Resistor	-	5 Ω
Transmit Flex Circuit	Transmission Line	10 cm [Note 1]	50 Ω
PZT5H Composite	Series Impedance	-	0.2184 - 2.7303i [Note 2]
	Transformer	Ratio 1: -71.7058 + 2.8637i [Note 2]	-
	Split Transmission Line (tx)	2π * 5 mm/8 x 0.5 mm x 59 μm	21 MRayl
	Split Transmission Line (rx)	75 μm x 0.5 mm x 59 μm	21 MRayl
Backing Layer	Parallel Resistance (tx)	2π * 5 mm/8 x 0.5 mm	8 MRayl
	Parallel Resistance (rx)	75 μm x 0.5 mm	8 MRayl
Matching Layer	Transmission Line (tx)	2π * 5 mm/8 x 0.5 mm x 26 μm	3 MRayl
	Transmission Line (rx)	75 μm x 0.5 mm x 26 μm	3 MRayl
Water Load	Parallel Resistance (tx)	2π * 5 mm/8 x 0.5 mm	1.48 MRayl
	Parallel Resistance (rx)	75 μm x 0.5 mm	1.48 MRayl
Rx Flex Circuit	Transmission Line	10 cm	50 Ω
Multiplexer Parasitics	Parallel Capacitor (active channel)	-	200 nF
	Series Resistance	-	2.5 Ω
	Parallel Capacitor (inactive channels)	-	180 nF
Amplifier Input Load	Parallel Resistor	-	50 Ω

Note 1: 10 cm transmission line is worst case; more likely length is 2 – 3 cm but simulation is based on worst case
Note 2: Series impedance and transformer ratio were calculated according to reference [23] using PZT-5H piezocomposite

to select a model compatible with future ASIC development, to minimize changes in modeling properties. By selecting a transducer/system model which can be fully converted into the electrical domain, it can be realized in pSPICE (Cadence Design Systems, Inc, San Jose, CA, USA) for detailed electronics simulation and used when determining the system response of the silicon design and comparing it with the mathematical model.

To simulate the electrical and acoustic properties of the piezoelectric transducer and its accompanying electrical circuitry, a KLM model was used [23], in conjunction with two-port electrical system modeling in MATLAB (The Mathworks, Cambridge, U.K.). Pre-existing modeling solutions such as Field II [24] or PiezoCAD (Sonic Concepts, Bothell, WA, USA) were considered, but because of the unusual geometry, separate transmitter, and receiver, and the desire to incorporate the full electronic pathway, an in-house solution was ultimately selected. Terminology and ABCD two-port parameter derivations from [25] were used in the simulation of the transducer and the supporting electronics. To properly reflect the different physical dimensions and element properties of the transmission (tx) and reception (rx) arrays, the system was modeled as two electroacoustic models, as shown in Fig. 2.

Using an ABCD two-port network implementation [26], the system in Fig. 2 was simulated with the values in Table I. The capsule diameter was assumed to be 10 mm at the radial center of the piezoelectric. Of particular note in this system, a multiplexer is integrated with each rx channel to allow synthetic aperture acquisition, and this has noticeable parasitic effects [27]. Multiplexing is handled in the digital circuitry

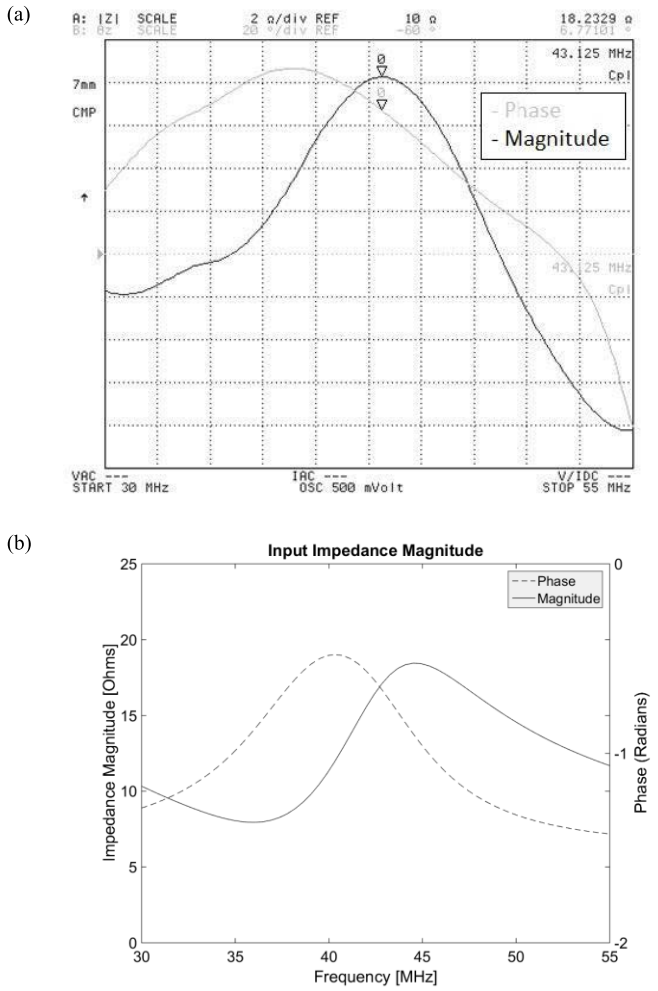

Fig. 3. Verification of KLM resonance calculations with experimental data. (a) Measured impedance curve (magnitude and phase) of the transducer with antiresonance marked. (b) Corresponding simulation results with matching antiresonance.

on the tx end, but must be placed before the analog front end in the rx circuit, so these effects should be modeled. The ADG706 (Analog Devices, Norwood, MA, USA) is a 16:1 multiplexer which was selected for the purposes of simulation and the specified input capacitance, path resistance and parasitic inactive channel capacitance can be incorporated as seen from Fig. 2.

To verify that the KLM modeling code developed is an accurate model of the expected system behavior, a single-element, physically focused lithium niobate μUS transducer designed to operate at 45 MHz [28] was modeled using the same methodology, and the resultant electrical impedance spectroscopy data were compared with measurements. We used a single-element transducer for validation because this configuration closely mimics the tx device that emerged from the simulation as appropriate. As shown in Fig. 3, the modeled results have an antiresonance peak at 44 MHz at an impedance of 18.4 Ω, while the experimental data show an antiresonance at 43.1 MHz at an impedance of 18.2 Ω, in good correspondence, thus supporting the model's ability to predict the electrical resonance behavior of the proposed system at μUS frequencies.

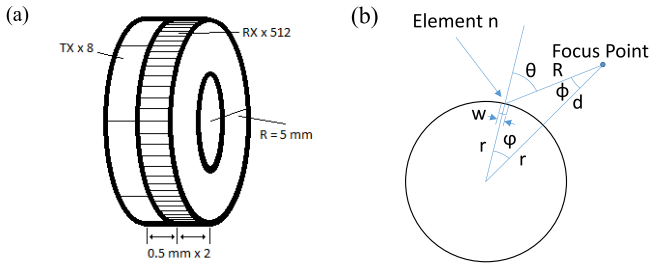

Fig. 4. Defined geometry for the curved array and the directivity. (a) Physical configuration of the tx and rx elements as simulated. (b) Effect of the curvature on the directivity calculation. Directivity values based on angle θ are used in the calculation of both suitable rx apertures and the weighting functions for received acoustic echoes. As the tx pulses are unfocused, no directivity is assumed on transmission.

IV. Ultrasound Array Geometry and Beamformer Design

The number and size of the elements in an array are key determinants of ultrasound system capability and complexity. In the circumferential array considered here, the tradeoff between system complexity and potential imaging performance caused by limiting the numbers of elements can be evaluated by calculating the active aperture that can be used for beamforming each radial image line, taking into account element directivity and array curvature. Increasing the total number of elements in the array, N_e, and correspondingly decreasing the element width w increases the active aperture size, which affects lateral resolution by improving the element directivity. The corresponding increase in the number of elements in the active aperture N_A also improves beamforming capability.

Large numbers of elements in the array will provide better image resolution than small numbers, but even moderate element counts (e.g., $N_e = 128$ elements) raise concerns about the realization of physical interconnects between the array and electronic circuitry. IVUS research has focused on arrays with $\leq$64 elements for this reason and due to space concerns [29]–[31]. Arrays with $N_e = 512$ elements are available commercially [32], but the relatively large number of elements raises additional concerns because of the volume of electronics required. To reduce this problem, the system defined here separates the tx and rx arrays [Fig. 4(a)] and requires only one tx and one rx channel to be active for each tx pulse. As full synthetic aperture approaches can have frame rate concerns, only eight tx elements are used, in a zone transmission configuration with synthetic aperture reception. Unfocused, plane wave transmission is used to fully insonate the area for each receive sequence. Each tx element comprised one eighth of the ring circumference, with the two transmitters adjacent to the active receiver used in each transmission. 512 elements are used in the rx array, in linearly stepped apertures dependent on the focal directivity. This arrangement necessitates additional multiplexing and adds a small amount of complexity to the interconnect scheme but the electronic circuitry is very much simplified overall and power consumption is also reduced. The unfocused tx scheme allows a single tx circuit to be used, and the synthetic aperture rx scheme allows only one rx front end to be active at a time,

reducing the rx power requirement by a factor equal to the aperture size.

Single-element transmission and reception can have a significant impact on the maximum scan rate of the system because of the need for multiple tx pulses to completely sample the aperture. The effect can be considered by taking into account the expected maximum rate of motion of the capsule during its passage. In a healthy human GI tract, the average rate of motion through the small bowel is approximately $v_{\text{avg}} = 0.17\text{mm} \cdot \text{s}^{-1}$ [33]. However, the motion can be highly pulsatile and variable, especially in patients with abnormalities, so much higher peak rates, $v_{\text{pk}} = 2-5$ mm s^{-1} [34], must be used for system design. Assuming an average sound propagation speed, $v = 1540$ ms^{-1}, a complete pulse-echo transit to a maximum radial depth of 10 mm outside the capsule is $t_{\text{pulse}} = 2 \times 10\text{mm}/1540$ m/s $= 13$ μs. Allowing time for additional scattering, $t_{\text{scan}} = 50$ μs, and taking $N_e = 512$ scan lines, a full B-scan image would take $t_{\text{total}} = N_e \times t_{\text{scan}} = 25.6$ ms, corresponding to a maximum frame rate $1/t_{\text{total}} = 39$ frames/s.

Even at the highest rate of motion through the bowel, $v_{\text{max}} = 5$ mm $\cdot$ s^{-1}, the capsule motion during a single frame is only $d = v_{\text{max}} \times t_{\text{total}} = 128$ μm. This corresponds to 2.08λ, where the wavelength in tissue, $\lambda = 1540$ ms^{-1}/25 MHz $=$ 61.6 μm, and thus represents a minor error in the B-scan field of view.

If a full synthetic aperture approach is used, the theoretical frame rate of 39 frames/s is further reduced by a factor equal to the number of elements in the imaging aperture, giving $\sim$1 frames/s if a 32 element aperture is implemented. Instead, our simulated results here are based on an important compromise in which, as noted, a large, defocused tx element is used in conjunction with individually sampled rx elements, allowing the frame rate of traditional imaging to be maintained while exploiting the reduction in electronic complexity offered by a synthetic aperture.

Because of the fixed o.d. of the capsule, the maximum number of elements in the active aperture can be calculated for a given focal distance based on the directivity function. The directivity function for a rectangular element can be expressed as [35]

$$\text{directivity} = \sin c(w \sin\theta/\lambda)\cos\theta \tag{1}$$

where w is the element width, θ is the angle between the array normal and the acoustic propagation vector in the plane of the image, and λ is the wavelength. Due to the curvature of the array, θ must be derived from the arc angle φ between the normal to the focus point and the active element normal [Fig. 4(b)]. For an acoustic target a distance d from the surface of an array of radius r, the distance R from the array element to the target can be found using the cosine law

$$R^2 = (r+d)^2 + r^2 - 2r(r+d)\cos\varphi. \tag{2}$$

The angle ϕ between segment R and d can, then, be obtained using the sine law

$$\frac{\sin\phi}{r} = \frac{\sin\varphi}{R}. \tag{3}$$

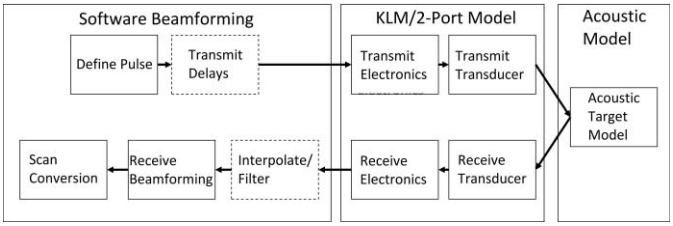

Fig. 5. Program flow for the ultrasound system simulation. The simulation is broken into three main components: the software beamforming, which performs the calculations which would be handled by the digital ASIC or base station in the full system; the KLM/two-port model, which models the effects of the analog electronic and mechanical elements of the system; and the acoustic model, which propagates the simulated pressure waves and models the reflectivity of the programmed targets.

Finally, the directivity angle is the sum of the two other angles as the outside angle of the third angle of the triangle (see Fig. 4)

$$\theta = \psi + \phi. \tag{4}$$

The results of the calculations from (2)–(4) are utilized by substituting them into (1) for each element. To avoid a contribution from noise at large angles for focal points close to the array, elements with directivity <0.8 are removed from the active aperture. A similar calculation is performed during simulation for each acoustic scatterer and the resultant directivity applied as a weighting function to the summation.

Using (1)–(4) and an estimated element width, $w = 0.8\ p$, where p is the array element pitch, the maximum aperture can be calculated for a focal distance from the array, $d_f = 5$ mm, which is the lowest value of the imaging window and the most difficult case for the directivity calculation. Given an array with $N = 512$ elements, an aperture size of 31 elements is obtained, which achieves a satisfactory compromise between minimum aperture size and electronic complexity. With a capsule o.d. of 10 mm, this gives $p = 61.4$ μm and $w = 49.1$ μm. The element separation is then 12.3 μm, similar to the smallest value physically possible with mechanical dicing of an array during fabrication [36], [37]. The tx elements are based on array of the same size, but with only eight elements of 3.93 mm in arc length. Initial values for the thickness of the active and matching layers were calculated at this point; however, they were adjusted through the simulation process and will be reported in Section V.

A MATLAB-based beamformer was created to interface with the KLM model, simulating the digital components of the proposed system, to allow virtual phantoms to be imaged. The beamformer is based on a classic delay-and-sum configuration with unfocused tx and dynamic rx beamforming [38], [39]. The full system data flow is broken into several discrete steps to allow simulation of different system specifications. As shown in Fig. 5, an initial tx pulse is defined as a single cycle, monopolar excitation at the target center frequency. The KLM/two-port model matrices are then applied to the input pulse to obtain the transmitted acoustic wave output at the water interface. This is then propagated using ray tracing to calculate the amplitude and delay of the echoes from the programmed acoustic scatterers as seen at the rx array elements.

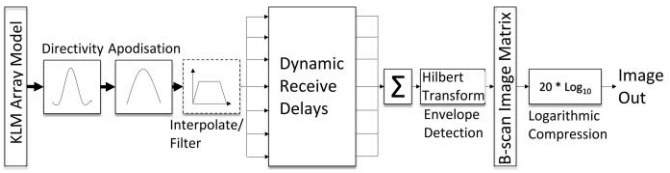

Fig. 6. MATLAB digital beamformer data flow. Data from the KLM model and acoustic phantom are stored in a matrix simulating the output from a full synthetic aperture scan and read into the beamforming algorithm in sets based on the programmed aperture size and step. The generated log-compressed image can be displayed as a linear image or can be subject to a Cartesian-to-polar conversion to display an anatomically correct image.

The resulting received echoes are multiplied through the KLM/two-port matrix model of the receiver, after which the amplitude and time quantization effects of a 12-bit, 100 MS/s analog-to-digital converter are applied. Simulating these digitization effects is particularly important as they can affect the accuracy of the beamforming delays and the resultant focal quality. Once the rx pulses have been processed through the KLM simulation and analog electronics models, they are passed through a digital rx beamformer to process the pulse-echo data and generate B-scan images (Fig. 6). The full set of synthetic aperture rx pulses is stored in a matrix and beamformed in sets determined by the selected aperture size and aperture increment. A set of rx focal points is determined, based on the minimum and maximum depths of the desired final image as well as the image resolution. The array configuration under test is then used to calculate the appropriate directivity from the elements in the active aperture to each of the rx foci. A Hanning apodization window is applied across the aperture before dynamic rx delays are applied to the received pulses within the active aperture. The delayed pulses are then summed and the resulting scan line is envelope detected using a Hilbert transform and added to the image buffer.

In addition to the steps listed in Fig. 6, optional interpolation and filtering can be applied between the apodization and dynamic rx beamforming operations. The active aperture is then incremented until all scan angles have been calculated, and the resulting B-scan is log-compressed and displayed with adjustable gray-scale resolution. A Cartesian-to-polar coordinate transformation is used to display the images in an annulus which mimics the GI tract anatomy for ease of interpretation by clinicians.

The simulated beamformer is designed to allow the aperture size, windowing, directivity cutoff, and other imaging parameters to be adjusted to assess the imaging abilities of the system. Initial imaging phantoms were created by defining point reflectors with individual reflection coefficients to assess axial and lateral resolution. Later, experimental data were used to allow more realistic image assessment.

V. Simulated System Performance

The response of a transducer was simulated using the KLM model with an applied single-cycle tx sinusoid centered at 25 MHz. As the intended final source for the tx excitation is an ASIC with limited slew rate, initial simulations of the digital drive suggested that the digital signal will more closely resemble a sinusoid than a square wave under capacitive drive conditions. Hence our approach mimics practical electrical excitation to a first approximation. The input impedances of individual tx and rx elements were then calculated for a frequency sweep from 0 to 50 MHz. These calculations were performed only on the piezoelectric components of the transducers and neglect the influence of the electrical components, showing the unloaded resonance behavior and electrical impedance of the transducers. Based on high performance piezocrystal commonly used in medical ultrasound imaging devices, a 40% by volume (1-x)[$Pb(Mg_{1/3}Nb_{2/3})O_3$]-x[$PbTiO_3$] (PMN-PT) 2–2 composite [40] was selected as the material of choice for simulation, and the geometric mean of the acoustic impedances was used to calculate the desired matching layer impedance. The thicknesses of the piezoelectric and matching layers were then adjusted to obtain a smooth resonance curve. After adjustment, a PMN-PT composite thickness of 85 μm and a matching layer 26 μm thick with an acoustic impedance of 4.08 MRayl produced the simulated impedance curves in Fig. 7(a) and (b). Of particular note is the significant difference in input impedance due to the difference in individual element size between the tx and rx arrays, which must be taken into account in the design of the corresponding electronics. The higher impedance seen in the receiver mirrors impedances which have been reported elsewhere [41].

The higher receive impedance can be handled in two ways in the receive system. For an electronic solution that is adaptable, such as an ASIC which is the most likely way to deal with the very small, high-frequency elements and the one we are developing, the input impedance can be designed to match the transducer impedance for maximized power transfer. However, in the circumstance that the electronics cannot be adapted to match the transducer to avoid power loss, adjustments may also be possible in the transducer design, including increasing the elevation dimension of the transducer to reduce the impedance proportionately without otherwise impacting the acoustic stack. If this is necessary for this design, the appropriate compromise between the elevation dimension and the overall device dimensions will be determined during experimental acoustic testing.

Once an acceptable pulse-echo response had been simulated, the 0.1-m transmission line specified in Table I was added to the tx and rx paths, as well as the rx multiplexer modeling. The two-way pulse-echo response between individual tx and rx elements was then calculated from an ideal point-scatterer target and the pulse bandwidth and time-domain pulse were plotted, as shown in Fig. 7(c) and (d). A bandwidth of 44% was calculated for tx–rx operation, with a center frequency of 24.9 MHz. The slightly lower bandwidth is due to increased difficulty in matching at higher frequencies with a large mismatch in transmit and receive transducer areas.

A virtual phantom was generated to assess the imaging resolution of the system and the effects of the defocused tx pulse. This had three ideal point reflectors located at (15 mm, 0), (20 mm, $\pi/10$), and in polar coordinates relative to the center of the array, the distances corresponding to the $f/2$, $f/3$, and $f/4$ positions as a function of the active aperture. These ideal point reflectors were used to assess the

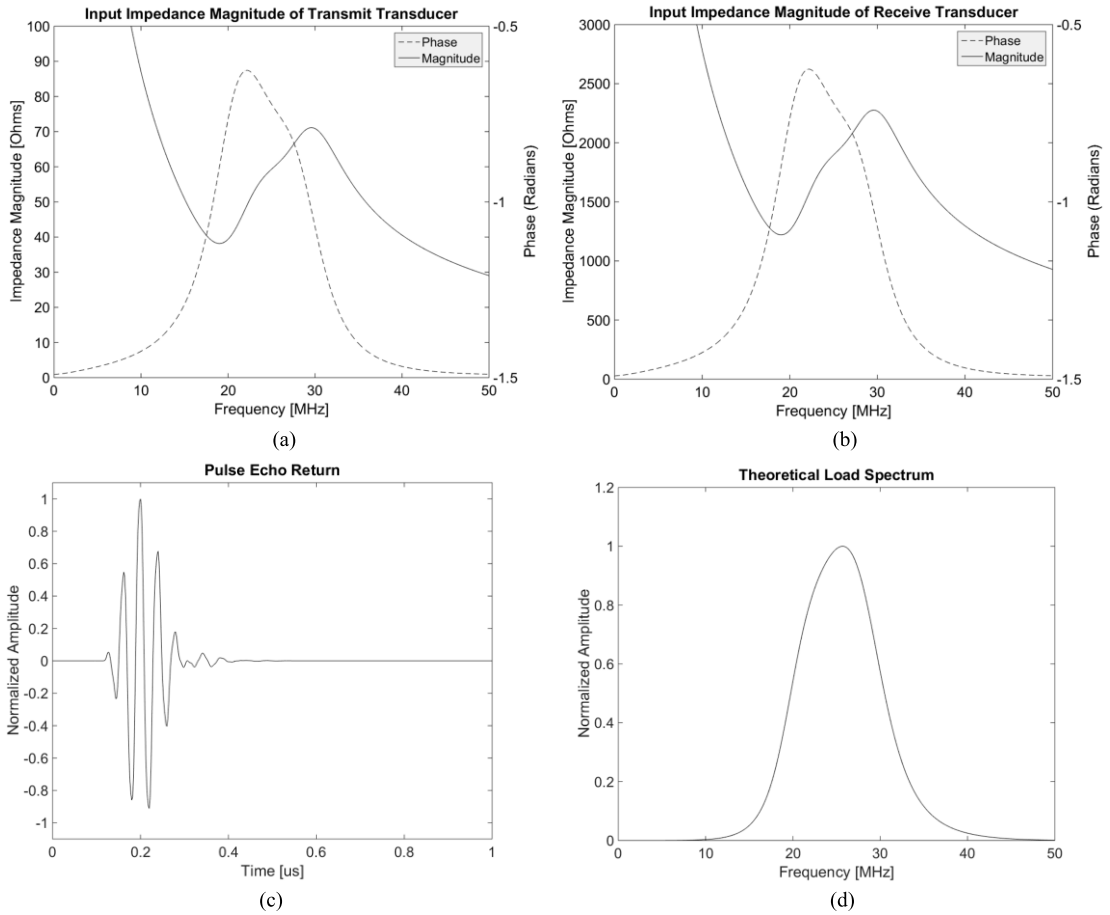

Fig. 7. KLM simulation results for the two-way tx–rx system. Input impedance magnitude for (a) tx and (b) rx transducers. The pulse-echo behavior is shown in the (c) time and (d) frequency domains. The impedance magnitude is much larger for the rx transducer than for the tx transducer principally because the rx transducer has a much smaller surface area.

impact of zone transmission on sidelobe levels. A virtual linear array scan was then performed with an aperture comprising 36 elements and a focal distance of 15 mm. The resulting B-scan was displayed with a dynamic range of 60 dB and standard log compression (see Fig. 8). The simulation was completed in 1 min 41 s and the three point targets had full-width half-maximum widths of 1.26×10^{-2}, 1.47×10^{-2}, and 1.74×10^{-2} rad, respectively. Given a wavelength of 61.6 μm at 24.9 MHz, this corresponds to lateral resolutions of 3.07λ, 4.77λ, and 7.06λ. This is wider than the theoretical ideal [38], but is expected given that the zone transmission configuration removes half of the normal focusing of delay-and-sum beamforming [42] and electronic parasitic effects further impact this. The axial resolutions were 160, 140, and 160 μm, respectively.

As the intended application of the array is to image tissue featuring well defined wall structures with relatively thin layers, a second virtual phantom was created to simulate two layers of material surrounding the array. The interfaces each consisted of 360 ideal reflectors positioned circumferentially and were separated radially by 1 mm. A sinusoidal variation in the distance from the array, between 13 and 18 mm, was added to mimic the irregularity of normal tissue layers. The resulting B-scan, Fig. 9, was produced in 22 min 24 s and shows clear resolution of the two walls.

To allow the generation of a virtual phantom with tissue layers and reflectivity similar to those in the human GI tract, a μUS image of porcine bowel tissue was acquired [43]; the porcine model was chosen as it closely resembles human tissue in scale and nature [44] and mechanical scanning with a single-element, μUS transducer was used to generate the data. Based on *ex vivo* tissue scans, this novel phantom was used instead of a standard simulation [24] due to the identified need to assess the system's sensitivity to specific target tissue.

Fresh-frozen porcine small bowel sourced from an abattoir was separated from the bowel wall along the long axis and perfused with 60 mL of degassed phosphate-buffered saline (PBS). The tissue was then pinned, mucosa uppermost (Fig. 10), on a platform comprising $\sim$30 mm of 1% agar (w/w) on top of ultrasound absorbing material (Aptflex F28, Precision Acoustics, Dorchester, U.K.), submerged in degassed PBS and scanned across the short axis of the bowel. A 45-MHz single-element transducer with a geometric focal distance of 6 mm (AFM Limited, Birmingham, U.K.) was mechanically scanned using a custom motor control and acquisition system programmed in LabVIEW (National Instruments, Austin, TX, USA) and the resulting A-scans were imported into MATLAB. These scans were then envelope detected, log-compressed and displayed in gray scale with the same beamformer architecture as the simulation code, as shown in Fig. 10(a). An example

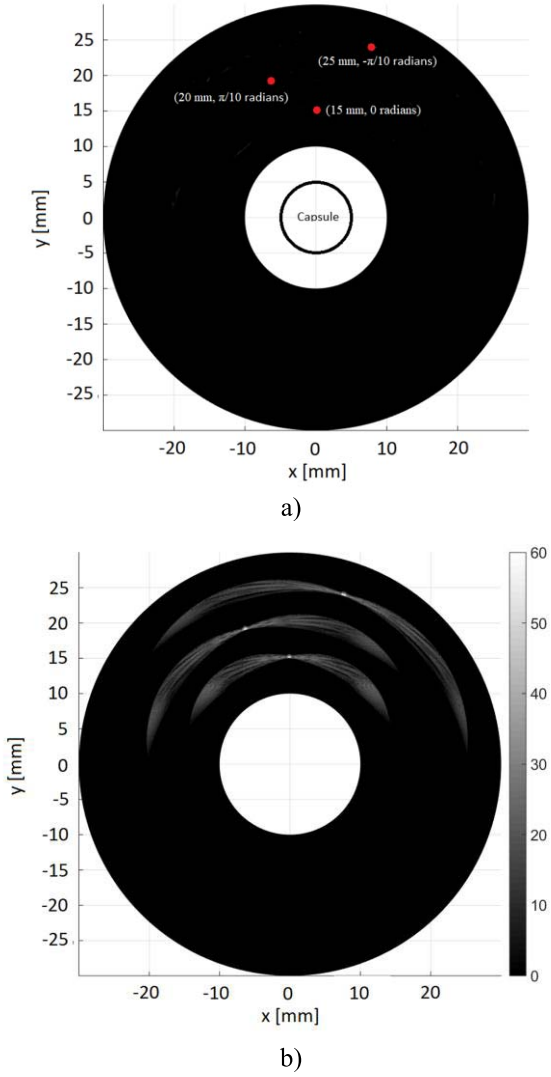

Fig. 8. Simulated B-scan image of three point targets at $f/2$, $f/3$, and $f/4$. (a) Simulated locations of targets with respect to the capsule. (b) Simulated B-scan displayed with 60-dB dynamic range.

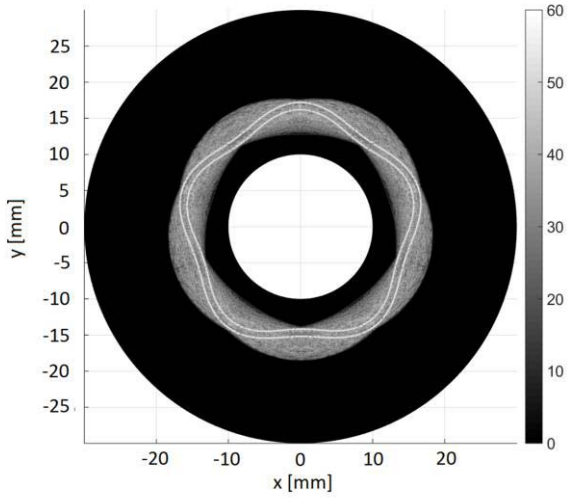

Fig. 9. Simulated B-scan image of two phantom walls with sinusoidal aberration created with 360 ideal reflectors each 1 mm apart, with 60-dB dynamic range.

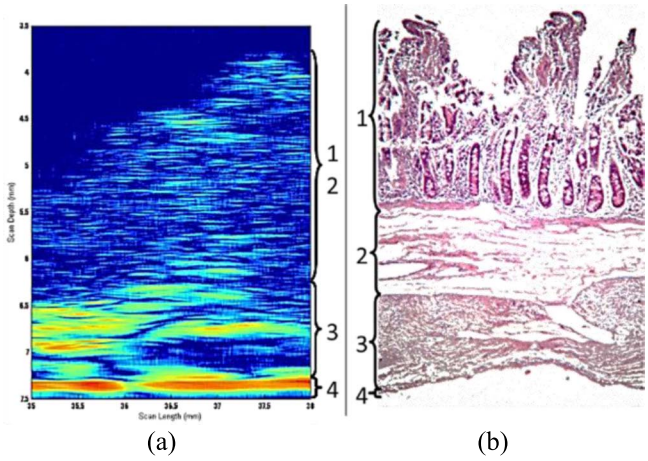

Fig. 10. (a) B-scan image of porcine small bowel recorded with focused 45-MHz single-element transducer mechanically scanned across the width of the bowel. Display is log-compressed with 60-dB dynamic range. (b) Hand E stained histological cross section of the bowel showing the same layers as (a). Tissue layers in (a) and (b) are 1—Mucosa (M), 2—Submucosa (SM), 3—Muscularis Propria (MP), and 4—Serosa (S).

stained cross section of the relevant tissue layers, representing standard anatomy, can be seen from Fig. 10(b) for comparison. While there is limited the literature on the acoustic impedance of the layers at this frequency, higher frequency measurements [45] show that there is minimal difference in the mechanical properties of the mucosa and submucosa in comparison to the other layers, supporting our finding of reduced contrast. The choice of μUS transducer frequency, 45 MHz, was made to ensure that all features expected to be visible with the 25-MHz array were represented in the simulation phantom.

Once an *ex vivo* image of sufficient quality had been obtained, the original annular section of the bowel was recreated by mapping the A-scan data into cylindrical coordinates. To reduce the effect of speckle in the phantom, a thresholding algorithm was applied to the data to produce four reflectivity levels at 10-dB intervals. A randomly generated set of 25 000 point scatters was then mapped onto the prelog-compressed data and assigned reflectivity values based on the echo strength of the underlying data. The resulting virtual phantom was then used as an input into the MATLAB beamformer and imaged using the simulated transducer array operating at 25 MHz. The B-scan image output from each of the three major steps in this process is shown in Fig. 11.

Comparing the layer structure seen from Fig. 11 with that of Fig. 10, the mucosa/submucosa, muscularis and serosa layers have retained their distinction. However, some loss of granularity is observed, as expected from the reduction in center frequency and tx defocusing. Clinical assessment indicated that the qualitative features had been successfully retained and that the image was of diagnostic quality.

VI. Discussion and Conclusion

With its very specific geometrical constraints and the need for μUS frequencies, USCE represents a new application of

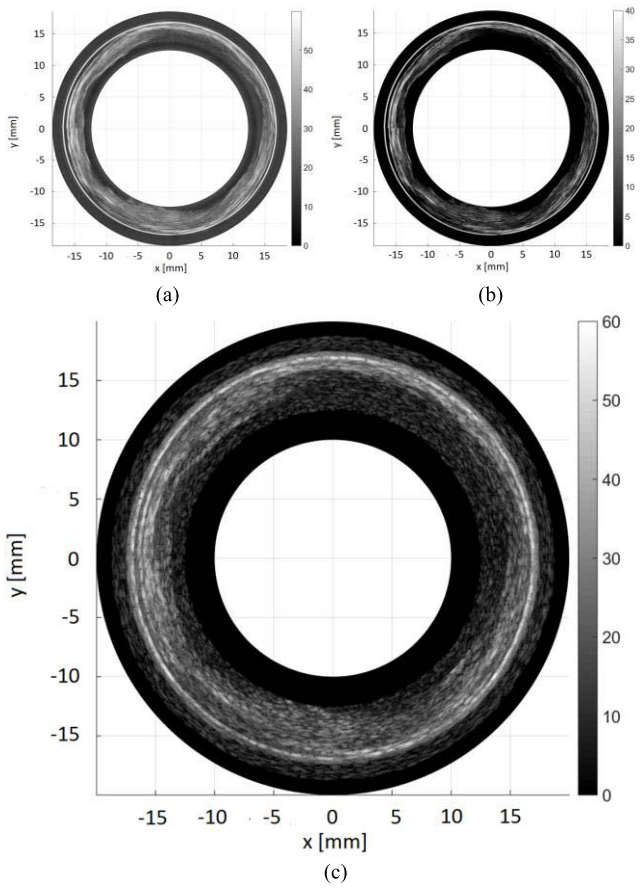

Fig. 11. (a) Reconstructed gray-scale image of the full length of dissected pig bowel from Fig. 10(a), digitally processed into a cylinder for conversion into a virtual GI tract phantom. The line shows where the image was stitched together to form a continuous loop. (b) Thresholded digital phantom with 4–10 dB stepped reflectivity ranges displayed in log-compressed gray-scale with 60-dB dynamic range. (c) Tissue image obtained from the virtual small bowel phantom with log-compression and 60-dB dynamic range.

ultrasound imaging, and therefore requires design procedures adapted from those used for other applications. This paper explains this adaptation. By integrating 1-D KLM modeling with a full digital beamformer implemented in MATLAB, a virtual system has been created to allow assessment of the electronic and acoustic performance of the proposed USCE systems and the effect of design variations on its output. For an example USCE tx–rx design, the calculation time of less than 2 min for resolution phantoms indicates that multiple design configurations may be tested and compared in a reasonable amount of time for effective virtual prototyping.

As the ultimate output of the virtual prototyping system, Fig. 11, representing results from a virtual porcine tissue phantom simulation, demonstrates a satisfactory correlation with the scan from *ex vivo* porcine tissue shown in Fig. 10. The broadening of the point-target sidelobes is expected because of the use of a defocused tx pulse. Similarly, the loss of resolution of the tissue phantom compared to the original scan, especially at the mucosal level, is also expected because of the reduced frequency of the USCE simulation. Nevertheless, sufficient resolution is achieved at 25 MHz to suggest a strong basis for USCE GI tract investigations and the other ultrasonic array and system parameters that were chosen have been demonstrated to be viable. The ability to distinguish layers is comparable to clinical work at 20 MHz [5], results are also comparable to previous work with mechanically scanned systems operating at 30 MHz [9].

The simulation method that has been described also holds considerable potential for exploration of other aspects of system design for USCE, such as potential operating frequencies, electrical parasitics, and system partitioning. Early modeling will provide a convenient means of evaluating a range of frequencies that are diagnostically appropriate and suitable for implementation in the USCE device. A commonly realized added benefit is the reduction in the time and engineering effort required to determine USCE parameters. This is especially attractive given the complex nature of future physical prototype USCE devices.

ACKNOWLEDGMENT

The authors would like to thank S. Sharma for supplying transducer data for the purposes of verification and R. Duncan for preparing and photographing the histology slide.

REFERENCES

[1] S. J. Spaner and G. L. Warnock, "A brief history of endoscopy, laparoscopy, and laparoscopic surgery," *J. Laparoendoscopic, Adv. Surg. Techn.*, vol. 7, no. 6, pp. 369–373, Dec. 1997.

[2] G. Ciuti, A. Menciassi, and P. Dario, "Capsule endoscopy: From current achievements to open challenges," *IEEE Rev. Biomed. Eng.*, vol. 4, pp. 59–72, Oct. 2011.

[3] M. J. Gora *et al.*, "Tethered capsule endomicroscopy: From bench to bedside at a primary care practice," *J. Biomed. Opt.*, vol. 21, no. 10, p. 104001, 2016.

[4] Z. Fireman, "Capsule endoscopy: Future horizons," *World J. Gastrointestinal Endoscopy*, vol. 2, no. 9, pp. 305–307, 2010.

[5] S. Ødegaard, L. B. Nesje, O. D. Lærum, and M. B. Kimmey, "High-frequency ultrasonographic imaging of the gastrointestinal wall," *Expert Rev. Med. Devices*, vol. 9, no. 3, pp. 263–273, May 2012.

[6] A. Fatehullah *et al.*, "Increased variability in ApcMin/+ intestinal tissue can be measured with microultrasound," *Sci. Rep.*, vol. 6, p. 29570, Jul. 2016.

[7] A. Moglia, A. Menciassi, and P. Dario, "Recent patents on wireless capsule endoscopy," *Recent Patents Biomed. Eng.*, vol. 1, no. 1, pp. 24–33, 2008.

[8] J. H. Lee *et al.*, "Towards wireless capsule endoscopic ultrasound (WCEU)," in *Proc. IEEE Int. Ultrason. Symp. (IUS)*, Sep. 2014, pp. 734–737.

[9] X. Wang *et al.*, "Development of a mechanical scanning device with high-frequency ultrasound transducer for ultrasonic capsule endoscopy," *IEEE Trans. Med. Imag.*, vol. 36, no. 9, pp. 1922–1929, Sep. 2017.

[10] J. Wang *et al.*, "Capsule ultrasound device: Characterization and testing results," in *Proc. IEEE Int. Ultrason. Symp.*, Sep. 2017, pp. 1–4.

[11] C. Liu, Y. Yan, L. Sun, Y. Chen, J. Dai, and W. Qiu, "A novel high-frequency endoscopic ultrasound system for colorectal cancer diagnosis," in *Proc. IEEE Int. Ultrason. Symp. (IUS)*, Jul. 2013, pp. 2045–2048.

[12] J. Schulze-Clewing, M. J. Eberle, and D. N. Stephens, "Miniaturized circular array [for intravascular ultrasound]," in *Proc. IEEE Ultrason. Symp.*, vol. 2. Oct. 2000, pp. 1253–1254.

[13] M. C. McDaniel, P. Eshtehardi, F. J. Sawaya, J. S. Douglas, and H. Samady, "Contemporary clinical applications of coronary intravascular ultrasound," *JACC Cardiovascular Intervent.*, vol. 4, no. 11, pp. 1155–1167, Nov. 2011.

[14] M. O'Donnell, M. J. Eberle, D. N. Stephens, J. L. Litzza, K. San Vicente, and B. M. Shapo, "Synthetic phased arrays for intraluminal imaging of coronary arteries," *IEEE Trans. Ultrason., Ferroelect., Freq. Control*, vol. 44, no. 3, pp. 714–721, May 1997.

[15] A. Sisman, M. Karaman, G. Gurun, and F. L. Degertekin, "Solid-state SL-IVUS arrays based on non-uniform aperture sampling," in *Proc. IEEE Ultrason. Symp. (IUS)*, Oct. 2010, pp. 1092–1095.

[16] H. S. Lay, V. Seetohul, B. Cox, C. E. M. Démoré, and S. Cochran, "Design and simulation of a high-frequency ring-shaped linear array for capsule ultrasound endoscopy," in *Proc. IEEE Int. Ultrason. Symp. (IUS)*, Sep. 2014, pp. 683–686.

[17] S. Cochran, C. E. M. Demore, and C. R. P. Courtney, "Modelling ultrasonic transducer performance: One-dimensional models," in *Ultrasonic Transducers: Materials and Design for Sensors, Actuators and Medical Applications*, 1st ed. Cambridge, U.K.: Woodhead Publishing, 2012.

[18] F. S. Foster, L. K. Ryan, and D. H. Turnbull, "Characterization of lead zirconate titanate ceramics for use in miniature high-frequency (20-80 MHz) transducers," *IEEE Trans. Ultrason., Ferroelect., Freq. Control*, vol. 38, no. 5, pp. 446–453, Sep. 1991.

[19] M. J. Zipparo, K. K. Shung, and T. R. Shrout, "Piezoceramics for high-frequency (20 to 100 MHz) single-element imaging transducer," *IEEE Trans. Ultrason., Ferroelect., Freq. Control*, vol. 44, no. 5, pp. 1038–1048, Sep. 1997.

[20] H. S. Lay, E. A. Simpson, G. Griffin, and G. R. Lockwood, "High-frequency annular array fabrication using a flex circuit matching layer," *Ultrason. Imag.*, vol. 34, no. 3, pp. 196–204, Jul. 2012.

[21] A. Sieg, "Capsule endoscopy compared with conventional colonoscopy for detection of colorectal neoplasms," *World J. Gastrointestinal Endoscopy*, vol. 3, no. 5, pp. 81–85, May 2011.

[22] H. S. Lay *et al.*, "Progress towards a multi-modal capsule endoscopy device featuring microultrasound imaging," in *Proc. IEEE Int. Ultrason. Symp. (IUS)*, Sep. 2016, pp. 1–4.

[23] R. Krimholtz, D. A. Leedom, and G. L. Matthaei, "New equivalent circuits for elementary piezoelectric transducers," *Electron. Lett.*, vol. 6, no. 13, pp. 398–399, Jun. 1970.

[24] J. R. A. Jensen, "A model for the propagation and scattering of ultrasound in tissue," *J. Acoust. Soc. Amer.*, vol. 89, no. 1, pp. 182–190, Jan. 1991.

[25] C. G. Oakley, "Calculation of ultrasonic transducer signal-to-noise ratios using the KLM model," *IEEE Trans. Ultrason., Ferroelect., Freq. Control*, vol. 44, no. 5, pp. 1018–1026, Sep. 1997.

[26] A. R. Selfridge and S. Gehlbach, "KLM transducer model implementation using transfer matrices," in *Proc. IEEE Ultrason. Symp.*, Oct. 1985, pp. 875–877.

[27] L. J. Busse, C. G. Oakley, M. J. Fife, J. V. Ranalletta, R. D. Morgan, and D. R. Dietz, "The acoustic and thermal effects of using multiplexers in small invasive probes," in *Proc. IEEE Ultrason. Symp.*, vol. 2. Oct.'1997, pp. 1721–1724.

[28] J. A. Brown, S. Sharma, J. Leadbetter, S. Cochran, and R. Adamson, "Mass-spring matching layers for high-frequency ultrasound transducers: A new technique using vacuum deposition," *IEEE Trans. Ultrason., Ferroelect., Freq. Control*, vol. 61, no. 11, pp. 1911–1921, Nov. 2014.

[29] F. L. Degertekin, R. O. Guldiken, and M. Karaman, "Annular-ring CMUT arrays for forward-looking IVUS: Transducer characterization and imaging," *IEEE Trans. Ultrason., Ferroelect., Freq. Control*, vol. 53, no. 2, pp. 474–482, Feb. 2006.

[30] E. D. Light, V. Lieu, and S. W. Smith, "New fabrication techniques for ring-array transducers for real-time 3D intravascular ultrasound," *Ultrason. Imag.*, vol. 31, no. 4, pp. 247–256, Oct. 2009.

[31] V. Patel, J. Dahl, D. Bradway, J. Doherty, S. Y. Lee, and S. Smith, "Acoustic radiation force impulse imaging (ARFI) on an IVUS circular array," *Ultrason. Imag.*, vol. 36, no. 2, pp. 98–111, Apr. 2014.

[32] M. Analoui, J. D. Bronzino, and D. R. Peterson, *Medical Imaging: Principles and Practices*. Boca Raton, FL, USA: CRC Press, 2012.

[33] J. E. Hall, *Guyton and Hall Textbook of Medical Physiology*, 12th ed. Amsterdam, The Netherlands: Elsevier, 2011, ch. 63.

[34] J. Worsøe *et al.*, "Gastric transit and small intestinal transit time and motility assessed by a magnet tracking system," *BMC Gastroenterol.*, vol. 11, p. 145, Dec. 2011.

[35] D. H. Turnbull and F. S. Foster, "Fabrication and characterization of transducer elements in two-dimensional arrays for medical ultrasound imaging," *IEEE Trans. Ultrason., Ferroelect., Freq. Control*, vol. 39, no. 4, pp. 464–474, Jul. 1992.

[36] A. Bezanson, R. Adamson, and J. A. Brown, "Fabrication and performance of a miniaturized 64-element high-frequency endoscopic phased array," *IEEE Trans. Ultrason., Ferroelect., Freq. Control*, vol. 61, no. 1, pp. 33–43, Jan. 2014.

[37] R. McPhillips *et al.*, "The fabrication and integration of a 15 MHz array within a biopsy needle," in *Proc. IEEE Int. Ultrason. Symp. (IUS)*, Sep. 2017, pp. 1–4.

[38] K. E. Thomenius, "Evolution of ultrasound beamformers," in *Proc. IEEE Ultrason. Symp.*, vol. 2. Nov. 1996, pp. 1615–1622.

[39] R. Mucci, "A comparison of efficient beamforming algorithms," *IEEE Trans. Acoust., Speech, Signal Process.*, vol. ASSP-32, no. 3, pp. 548–558, Jun. 1984.

[40] Z. Qiu *et al.*, "Characterization of piezocrystals for practical configurations with temperature-and pressure-dependent electrical impedance spectroscopy," *IEEE Trans. Ultrason., Ferroelect., Freq. Control*, vol. 58, no. 9, pp. 1793–1803, Sep. 2011.

[41] M. Lukacs *et al.*, "Performance and characterization of new micromachined high-frequency linear arrays," *IEEE Trans. Ultrason., Ferroelect., Freq. Control*, vol. 53, no. 10, pp. 1719–1729, Oct. 2006.

[42] I. K. Holfort, F. Gran, and J. A. Jensen, "P2B-12 minimum variance beamforming for high frame-rate ultrasound imaging," in *Proc. IEEE Ultrason. Symp.*, Oct. 2007, pp. 1541–1544.

[43] T. Anbarasan *et al.*, "High resolution microultrasound (μUS) investigation of the gastrointestinal (GI) tract," in *Biosensors and Biodetection: Methods and Protocols: Electrochemical, Bioelectronic, Piezoelectric, Cellular and Molecular Biosensors*, vol. 2, B. Prickril and A. Rasooly, Eds. New York, NY, USA: Springer, 2017, pp. 541–561.

[44] L. Schantz, K. Laber-Laird, S. Bingel, and M. Swindle, *Essentials of Experimental Surgery: Gastroenterology*. Boca Raton, FL, USA: CRC Press, 1996.

[45] C. S. Jørgensen, J. E. Assentoft, D. Knauss, H. Gregersen, and G. A. Briggs, "Small intestine wall distribution of elastic stiffness measured with 500 MHz scanning acoustic microscopy," *Ann. Biomed. Eng.*, vol. 29, no. 12, pp. 1059–1063, Dec. 2001.

Holly S. Lay (S'11–M'11) received the B.Sc. degree in electrical engineering and the Ph.D. degree in engineering physics from Queen's University, Kingston, ON, Canada.

After working in industry for two years, she joined the Institute for Medical Science and Technology, University of Dundee, Dundee, U.K., as a Post-Doctoral Researcher on the Sonopill Programme in 2013. She is currently a Post-Doctoral Research Associate with the Department of Engineering, University of Glasgow, Glasgow, U.K. Her research interests include high-frequency ultrasound, ultrasound electronic systems, and ultrasound device miniaturization.

Benjamin F. Cox received the B.Sc. degree in biology from Dalhousie University, Halifax, NS, Canada, and the M.D. degree from the First Faculty of Medicine, Charles University, Prague, Czech Republic, in 2010.

He is currently a Clinical Fellow on the Sonopill Programme with the Life Sciences Department, University of Dundee, Dundee, U.K. He has been involved in numerous research projects with more recent involvement in interventional MRI and ultrasound capsule endoscopy. His research interests include medical imaging, gastroenterology, and inflammation.

Vipin Seetohul (S'04–M'05) received the B.Eng. degree (Hons.) from the University of Liverpool, Liverpool, U.K., the M.Sc. degree from Imperial College London, London, U.K., the M.Phil. degree from the University of Bath, Bath, U.K., and the Ph.D. degree from the University of Warwick, Coventry, U.K.

In 2013, he joined the Sonopill Programme at the University of Glasgow, Glasgow, U.K., where he was a Post-Doctoral Research Associate in microultrasound and capsule endoscopy. Since 2017, he has been a Product Development Manager with Micrima Ltd., Bristol, U.K. His research interests focus on medical devices innovation and development.

Dr. Seetohul is a member and ambassador of The Institution of Engineering and Technology and the Institute of Physics and Engineering in Medicine.

Christine E. M. Démoré (S'01–M'07) was born in Australia in 1978. She received the B.Sc. degree in engineering physics and the Ph.D. degree in physics from Queen's University, Kingston, ON, Canada, in 2000 and 2006, respectively.

Since 2007, she has been with the Institute for Medical Science and Technology, University of Dundee, Dundee, U.K., where she is currently a Scientist in physical sciences with the Odette Cancer Research Program, Sunnybrook Research Institute, and has been an Assistant Professor with the Department of Medical Biophysics, University of Toronto Toronto, ON, since 2016. Her research interests include the development of ultrasonic devices to enable emerging biomedical applications, such as acoustic particle manipulation and clinical adoption of microultrasound imaging.

Dr. Démoré is a member of the Institute of Physics. She was a recipient of the IEEE Ultrasonics Young Investigator Award in 2015. Since 2013, she has held the Royal Society of Edinburgh/Caledonian Research Foundation Biomedical Personal Research Fellowship.

Sandy Cochran (A'01–M'01) received the B.Sc. degree in electronics and computing, the M.B.A. degree in enterprise networks, and the Ph.D. degree in electrical engineering from the University of Strathclyde, Glasgow, U.K.

He is currently a Professor of ultrasound materials and systems with the School of Engineering, University of Glasgow, Glasgow, having previously held posts in engineering, physics, and medicine at several other Scottish universities. He has coauthored over 300 journal and conference papers and presentations. His research interests include devices and systems for ultrasound in medicine and life sciences, new piezoelectric materials and better utilization of existing materials, microscale and miniature devices for new applications including microultrasound imaging, focused ultrasound surgery and ultrasound-targeted drug, and ultrasound systems for intraluminal imaging of the gut and for manipulation of cells and particles.

Dr. Cochran is a member of the U.K. Institute of Engineering and Technology, and a fellow of the U.K. Institute of Physics.